The Leading Proton Spectrometer of ZEUS

Roberto Sacchi
Università di Torino and INFN

Abstract

Starting in late 1993, the ZEUS experiment at HERA has operated a Leading Proton Spectrometer (LPS). The protons scattered at small angles and carrying a substantial fraction of the incoming proton momentum were detected in six stations equipped with silicon microstrip detectors positioned very close to the proton beam, between 20 and 90 meters from the interaction vertex. The track deflection induced by the proton beam magnets was used to determine the scattered proton momentum.

The LPS was operated continuously up to the end of year 2000, when the HERA straight section had to be rebuilt to increase the specific luminosity. The experimental setup, the performance of the detector, the track reconstruction and the analysis techniques are reviewed in this paper.

1 Introduction

The original motivation for the Leading Proton Spectrometer (LPS) at HERA was the result of the work on leading proton physics carried at CERN ISR [1], in which the properties of the hadronic states in proton-proton interactions were studied after removing the leading proton momentum, (here, *leading* means taking a greater than the average share of the available energy).

Since its installation in the ZEUS experiment, new interesting fields opened up in diffractive physics which further emphasized its importance. Nonetheless, the detector was designed to cover a broad range of proton momenta, ranging from purely elastic *ep* scattering down to target fragmentation in DIS.

The spectrometer was formed by placing detectors within the HERA beam elements along the first 90 meters from the interaction vertex. Roman pots [2] were used to position the detectors in close proximity to the circulating proton beam.

Since the accessible phase-space was squeezed between the 10σ profile of the beam and the vacuum chamber limits, lot of efforts were devoted in optimizing the number and the position of the detector stations within the constraints of finance and practicability so as to piece together a reasonable acceptance. The detectors had to be large in size and shaped to fit closely the elliptically-shaped beam. Custom front-end electronics had to be developed to work as close as 9 cm from 1 MJ of stored proton beam energy, pipelining and buffering data 90 m away from the acquisition system. A mechanical system capable of retracting detectors and pots during the beam fills and automatically reinserting them with good position accuracy during beam collisions had to be designed, together with a fast extraction safety system to avoid detector damage. Finally, an alignment, calibration and reconstruction method had also to be developed.

This paper gives a description of the spectrometer and its layout, of the alignment, calibration and reconstruction method and summarizes the performance of the detector in six years of data taking. For additional details on ZEUS and on the LPS, please refer to ref. [3].

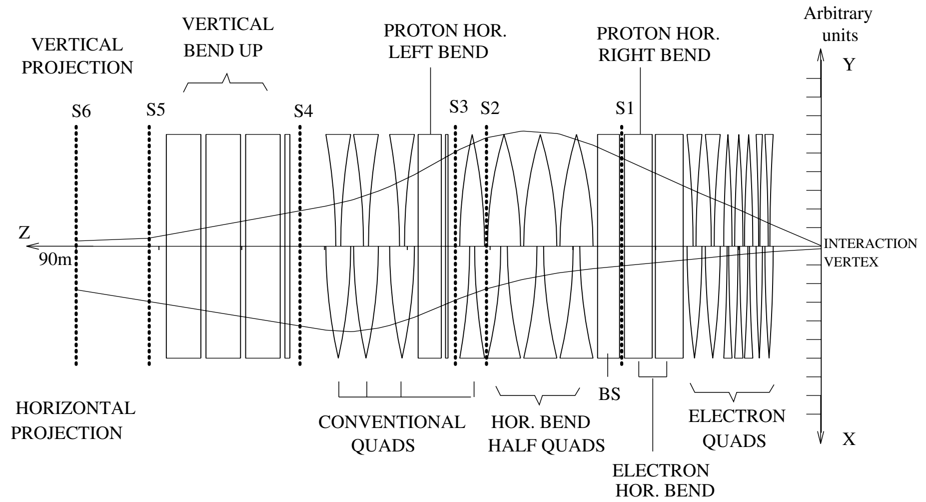

Fig. 1: Layout of the proton beam optics from the interaction vertex down to 90 m in the proton direction. The optical function of each beam element is shown. The curves represent the vertical (above) and horizontal (below) projection of the beam envelope. The position of the six detector stations is also shown as a dashed line.

2 Beam optics

Figure 1 is a simplified layout of the proton beam optics of the old[1] HERA straight section showing the optical function of the beam elements and the position of the six detector stations. The beam-line starts with a set of weak quadrupole magnets which focus the electron beam. Their effect on the proton beam is reduced by the ratio of the beam energies $E_e/E_p = 27.5/820 \sim 0.03$ but must be taken into account. Then follow two horizontal bending magnets which sweep the electron beam away from the proton beam. When protons arrive at the first station S1, the net effect is just a deflection of ~ 2 mm, whose direction depends on whether positrons or electrons are stored in the collider.

Immediately after S1, a septum magnet BS deflects the proton beam horizontally toward the outside of the ring and the deflection is further increased by the three magnetic half-quadrupoles which follow. Here is placed station S2 and, after the next conventional quadrupole, station S3. Here also ends the horizontally-bending section of the spectrometer, where the beam has been deflected horizontally by a distance of 15.8 mm.

Following S3 there is a horizontal bending magnet which brings back the proton beam parallel to its initial direction. A further three conventional quadrupoles completes the focusing system of the straight section. Finally comes the vertically-bending section of the spectrometer composed by stations S4 to S6 with three bending magnets in between and a total of 5.8 mrad bending angle.

Not shown in the figure are the horizontal and vertical orbit correction coils which were manually steered to optimize the luminosity in each fill; as their effect on the proton beam was not negligible, their current intensities were added to the LPS data stream for offline correction. Also, beam position monitors were installed close to stations S3 and S4 which were used by the LPS safety system to detect beam instabilities.

Figure 1 also shows the 10σ envelope of the beam in the horizontal and vertical plane. The detector shapes were matched to these profiles and therefore varied between different stations. The intrinsic transverse momentum spread of the proton beam at the interaction vertex had an rms of about 50 MeV horizontally and 100 MeV vertically.

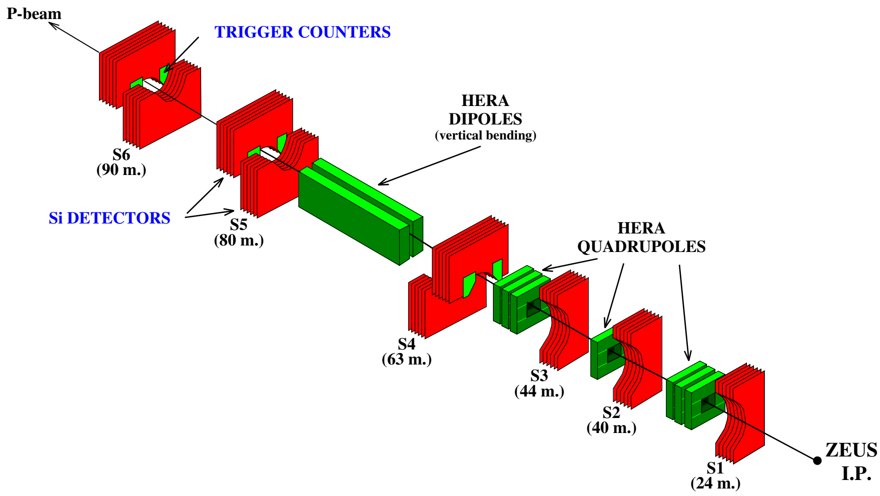

Fig. 2: Artistic view of the leading proton spectrometer from the ZEUS interaction point (I.P.) up to the last detector station. The drawings of the detectors are not to scale.

3 Spectrometer layout and construction

The layout of the LPS is schematically drawn in figure 2; it consists of six detector stations (S1 to S6) displaced along the beam line in the direction of the outgoing protons at the distances (measured from the interaction vertex) shown in the figure.
Each of the stations S1, S2 and S3 is equipped with an assembly of six planes of silicon microstrip detectors parallel to each other and mounted on a mobile arm which allow them to be positioned near to the proton beam by moving horizontally, from the outside of the HERA ring toward the ring center. The detector planes are inserted in the HERA beampipe by means of re-entrant Roman pots, stainless steel cylinders with an open end away from the beam and the other end closed. The silicon detectors are inserted from the open end and are moved until they are at about 0.5 mm from the closed end. The whole pot can be then inserted transversely into the beampipe.
Stations S4, S5 and S6 each consist two halves, each half containing an assembly of six planes similar to those of S1,S2 and S3. They are also mounted on mobile arms which can be moved and independently approach the beam from above and from below. In the operating position the upper and the lower halves partially overlap (cf. figure 5a). The offset along the beam direction between the upper and the lower pots is approximately 10 cm. The upper halves contain additional planes used for the trigger system.

In total, the LPS features 60 silicon planes and about 54000 readout channels.

3.1 Detectors and Front-end

The basic front-end element is shown in figure 3. It consists of a shaped detector plane with up to 1024 strips mounted on a Cu-Invar multilayer printed circuit board which matches the coefficient of thermal expansion of the silicon. This board also carries the front-end readout chips and features thin layers of copper for thermal conduction and cooling vias which provide metal conducting paths from the metal planes to the exterior. Water cooled pipes of 1 mm^2 are also shown which are mounted in thermal contact with these vias.
In each pot, six of these units are closely packed together, mounted with their normal parallel to the beam. Detector strips are oriented at $0°$ and $\pm 45°$ relative to the pot axis, two planes for each orientation, to provide redundancy and to remove reconstruction ambiguities. An additional unit is added in some pots with smaller planes used for the trigger system. A picture of the assembly mounted on the support is shown in figure 4. The distance between neighboring planes is approximately 7 mm, therefore the overall

[1] In year 2001 the straight section of HERA was redesigned to achieve an increased specific luminosity.

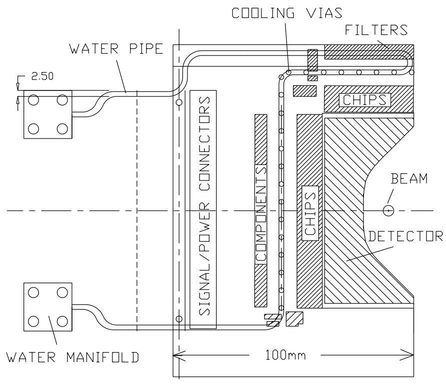

Fig. 3: Plan view of a detector plane mounted on the support board with indications of the chip, component layout and the cooling system.

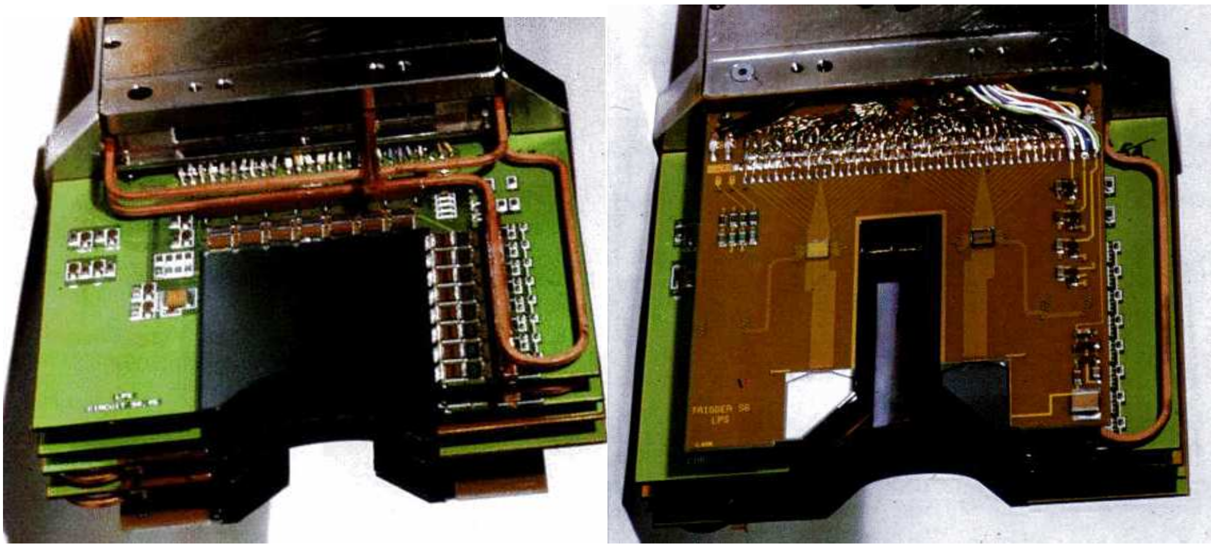

Fig. 4: Detector assembly mounted on the support as seen from two opposite sides (only four planes out of six were installed for this picture). The small trigger planes are clearly visible in the picture on the right.

thickness of the assembly is only about 5 cm. The detector planes are mounted in each assembly with a precision of about 30 μm. In the final arrangement, the detector packet is enclosed in a box which fits the shape of the detectors and provides both mechanical and electromagnetic protection; it is made of a thin copper layer enclosed in epoxy with a total thickness of 300 μm.

The detectors planes are 300 μm thick single-sided microstrip planes with up to 1024 p+ strips implanted on the n+ silicon substrate. The interstrip distance is 115 μm for the detectors with strips oriented at 0° and $115/\sqrt{2} = 81$ μm for the detectors with strips at $\pm 45^\circ$. Typical depletion voltages range between 35 and 50 V; at these voltages, the strip capacity is about 1.2 pF/cm with a leakage current of few nA[2]. The size of the detectors vary between different stations but is approximately 6×4 cm^2. The precision of the elliptical shaped cut, which also vary from station to station, was measured to be of the order of 100 μm. In data taking conditions the distance of each detector plane from the beam center ranges between 3 and 20 mm depending on the station.

The frontend readout electronics [4] was designed based on a set of specifications derived from the HERA environment and from the pipelined readout architecture of the ZEUS experiment. In particular,

[2] Some of the detector planes showed ageing effects leading to hundreds of nA of leakage current after six years of operations.

radiation hardness to high energy protons and neutrons, low noise and low power consumption were required. The ability to sustain large input currents from the DC coupled silicon detectors without large loss of gain was also crucial in the design. As a result, a mixed technology combination is used: a bipolar amplifier-comparator VLSI chip (TEKZ) followed by a CMOS digital pipeline and multiplexer chip (DTSC), with each chip serving 64 strips. The system is binary, i.e. a bit is stored for every channel in the time slice corresponding to a bunch crossing, which is set if the pulse height exceeds a threshold, and is zero otherwise. No other information is kept.
The TEKZ chip [5, 6] integrates a preamplifier followed by a comparator with a common programmable threshold. The shaping time is τ_s=32 ns and the overall gain is about 150 mV/fC. The amplifier noise scales linearly with the load capacitance C and was measured to be $\sigma_n = 690 + 40C$ [e$^-$]; even for the longest strip, the ratio signal over noise is over 20. The chip also features four calibration lines, each connected to the calibration capacitors of 16 channels, allowing to inject a known charge in each channel. The power consumption is about 2 mW/channel.
The task of the Digital Time Slice Chip (DTSC) [7, 8] is to buffer the digital data until a trigger decision is made and to multiplex the data out serially on four data lines. It features a level-1 digital pipeline, 64 cells wide, which operates synchronous with the 10.4 MHz collision frequency and stores the data long enough to allow for the 5 μs latency of the ZEUS level-1 trigger decision. A level-2 buffer is also available. The power consumption is also about 2 mW/channel.

3.2 LPS Trigger

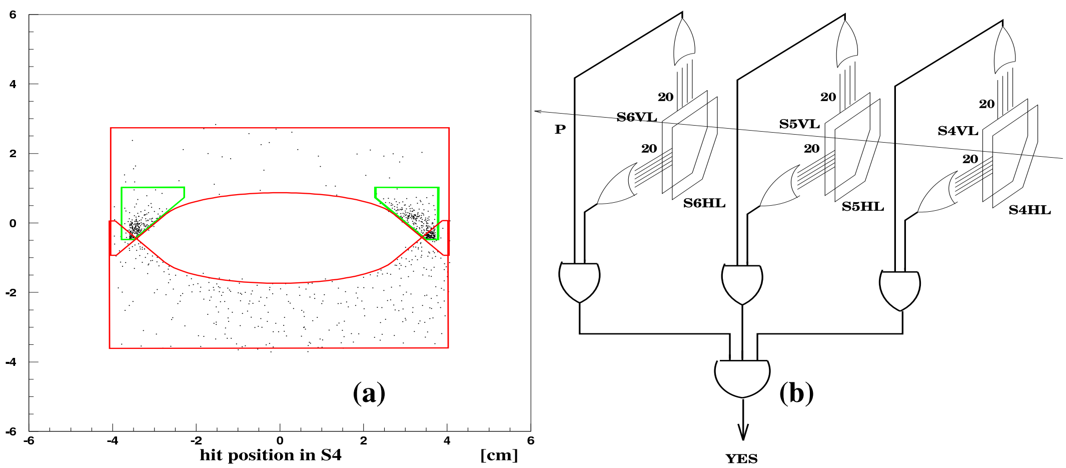

Fig. 5: (a) Hit positions in station S4: the outlines of the LPS detectors and of the two small trigger planes are shown. (b) Trigger logic implemented online; only left side is shown.

A trigger system [9] was designed in stations S4-S6 to tag elastic and diffractive events where the scattered proton carry a fraction of the beam momentum x_L larger than 0.95. Because of the large vertical transverse momentum spread of the beam in the interaction region, these events cluster in two opposite narrow regions in the left and right inner corners of the LPS detectors. To cover this area, μstrip silicon trigger planes were designed as small trapezoids (see figure 5a). Two planes are installed in each corner of the upper pots which overlap in position and have orthogonal strip orientation (0° and 90° relative to the pot axis). Each trigger plane is segmented into 20 strips with 750 μm strip pitch and is AC coupled to a TEKZ chip. The digitized data are sent in parallel 100 m away where the trigger logic is implemented in FPGA units. Here, a matrix trigger logic was designed where linear correlations can be required between hit positions to provide momentum selection. The simpler logic shown in figure 5b, corresponding to a coincidence of hits in all the three stations, has been used in the final implementation.

The typical rate of triggers has been a few kHz at most, reducing to few Hz when some activity in the ZEUS central detector was required in conjunction.

3.3 Mechanical Construction

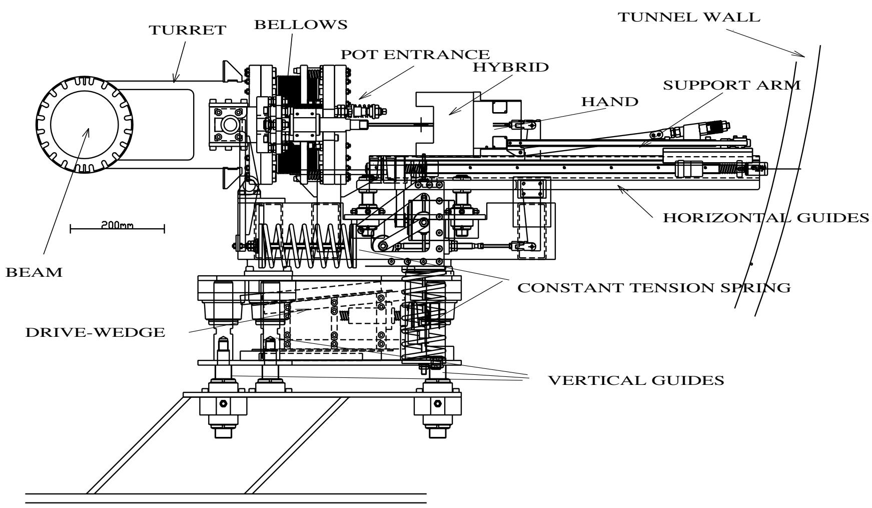

Fig. 6: Line drawing of the mechanical construction of a horizontally moving pot.

Roman pots allow to operate the detectors at atmospheric pressure and to easily retract them in a safe position during machine fill or when beam instabilities occur. The pot lateral walls are 3 mm thick while, at its end nearest to the beam, the pots are only 0.4 mm thick and are shaped around the detector cutout so that the pot can fit snugly against the beam profile. Thin windows, 0.4 mm thick, are also let into the upstream and downstream sides of the pot to reduce multiple scattering.

Figure 6 is a labeled line-drawing of a horizontally mounted pot system. The detectors, support hand and arm are mounted on a small carriage and move on the horizontal guide by a step-motor drive. The pot itself can be positioned nearer or further from the beam and has also limited lateral movement provided by a wedge and guide system; to ensure vacuum tightness and allow such movements, a bellow connects the pot to the vacuum pipe. The atmospheric force on the pot amounts to about 8 kN and is balanced by a constant tension spring system with two springs, a force summing system in a triangular frame and a system of levers to apply the force to the pot flange. The pot position is measured with resolvers mounted on the motor shaft with a nominal resolution of 5 μm.

Stations S5 and S6 somewhat differ in the design because they were inherited and modified from previous experiments at CERN [10]. In particular, to balance the atmospheric force, a pneumatic system with high pressure nitrogen is used. The pots are driven with DC motors and the pot positions are measured using linear transducers with a resolution of about 30 μm.

4 Detector operations, performance and acceptance.

The insertion of the pots and the detectors is a critical task which begins after the beams are brought in collision and stable conditions are observed.
An automatic insertion program was developed. First, all the detectors are moved simultaneously into the pots. Later, one pot a the time is moved in steps of decreasing size (from 2 to 0.1 mm) into the operating position. Prior to the insertion, the program checks the proton beam positions measured by the HERA beam position monitors, the positions and rates of the HERA collimators, the rates of the C5 counter and those of the trigger counters of a neutron calorimeter [11] which is located 10 m downstream of S6. These quantities, together with the rates of the LPS trigger planes and of some additional scintillators

positioned around the beampipe are also continuously monitored during the insertion. The insertion stops if any of these quantities exceeds a threshold and is recovered when the corresponding value decreases to a safe level. If several stops occur, the procedure is aborted and the pots are extracted. Otherwise, when all the pots are in the operating position, the procedure stops. During data acquisition, the proton beam positions and the LPS trigger rates are continously monitored and a hardware safety system triggers a fast extraction of the detectors if the rates are above a programmable threshold or if the beam drifts away from its nominal position.

25 minutes or longer time were necessary to insert the pots, depending on the beam conditions. This, and the fact that the beam conditions did not always allow a safe insertion of the detectors results in a reduced efficiency compared to other components of the ZEUS detector.
A total integrated luminosity of 72 pb^{-1} was collected by the LPS from 1994 to 2000, which should be compared to the 130 pb^{-1} collected by ZEUS in the same years. A breakdown is shown in table 1. The integrated luminosity used in physics analyses (also shown in the table) was 14% lower because some HERA fills with very unstable beams, high background or bad detector conditions were excluded.

Table 1: Integrated luminosity collected by ZEUS and by the LPS. The column marked with an asterisk is the luminosity which is used in physics analyses.

	Luminosity (pb^{-1})				Luminosity (pb^{-1})		
Year	ZEUS	LPS	LPS*	Year	ZEUS	LPS	LPS*
1994	3.0	0.9	0.9	1997	28	14	13
1995	6.6	3.5	3.4	1999	36	15	10
1996	11	4.0	0.0	2000	47	35	35
Total					132	72	62

Note that the inefficiency caused by detector problems was negligible compared to that caused by bad beam condition and was mainly due to mechanical problems in the pot positioning system or dirt in the cooling water blocking the small pipes of cooling system. Few planes showed occasionally strong increase in leakage current or dead readout DTSCs and were replaced when possible during the machine shutdowns which occurred once per year. Fortunately, the system was designed with sufficient redundancy that the loss of one or even two planes in a pot without immediate replacement can be tolerated. Excluding the malfunctioning planes, the noisy or malfunctioning channels were always less than 2% and were masked in the readout. The efficiency for the remaining channels was measured to be better than 99.5% in each plane. An average noise of less than 0.3 channels firing in each plane in a time slice corresponding to a bunch crossing was measured under data taking conditions by examining collisions of empty electron and proton bunches.

Figure 7a shows the acceptance coverage of any coincidence of 2 stations in S4, S5 and S6 for different values of the fractional momentum x_L as a function of the transverse components p_X and p_Y of the proton momentum. The odd shape of the regions covered by the detectors reflects the shape of the detectors and the shape of the beam apertures, both distorted by the effect of the magnetic fields.
For $x_L = 1$ protons, i.e. for elastic and diffractive interactions, the acceptance is small and limited to the two narrow bands at $p_X > 0$ and $p_X < 0$ shown in the figure. These regions correspond to the two inner corners of the detectors (see figure 5a) and map into $0.25 \lesssim p_T \lesssim 0.7$ GeV. Note that a large part of this region is covered by all the three stations; in diffractive events, about half of the tracks hit all the three stations.
At lower energies, protons which are produced at low p_T and are inside the angular spread of the beam can be detected because the bending magnets sweep them away from the beam. Here the acceptance is larger and extends up to $p_T = 1$ GeV and down to $p_T = 0$, depending on the proton momentum; unlike

at $x_L = 1$, the large majority of events are two-station tracks.
The acceptance as a function of x_L and p_T is shown in figure 7b. Averaging over the transverse momentum by assuming a typical exponential p_T^2 distribution, the acceptance for diffractive events is few percent, increasing to up to 50% at $x_L \sim 0.8$, depending on the slope of p_T^2 distribution.

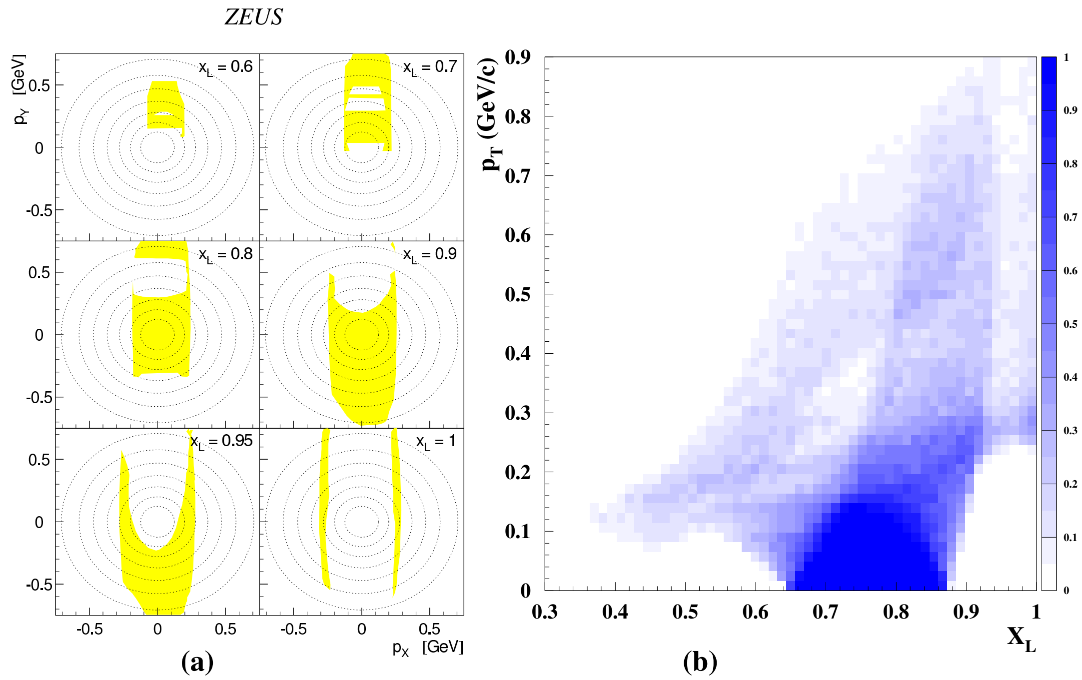

Fig. 7: (a) Transverse phase space of the scattered proton covered by any coincidence of 2 stations in S4$\rightarrow$S6 for fixed fractional momentum x_L. The multiple scattering on the pot walls and the finite size of the interaction vertex smear the acceptance along the contours of these region. (b) Acceptance of any coincidence of 2 stations in S4$\rightarrow$S6 as a function of x_L and the proton transverse momentum p_T.

In comparison, the acceptance of S1,S2 and S3 is complementary and has very little overlap with the acceptance of S4, S5 and S6. It extends down to $x_L = 0.3$ and contributes at larger p_T, but is smaller at $x_L = 1$. In addition, the acceptance is reduced when the machine operates with positrons rather than electrons because the proton beam is shifted in an unfavored position at the location of S1; this was unfortunately the dominant operating mode of HERA after 1993.

5 Reconstruction and alignment of the detector

5.1 How the Proton Momentum can be Measured

Figure 8 shows a simplified layout of the LPS beam optics. The two groups of stations S1-S2-S3 and S4-S5-S6 form two independent spectrometers with almost no acceptance overlap. As shown in the figure, they exploit the horizontal and vertical bending sections of the beam line.
In the simplest case of a track being recorded in the three stations S4-S5 and S6 (see figure 8), the track projection on the horizontal plane is a straight line while the track deflection d_v in the vertical bending magnets between S4 and S5 gives a direct momentum measurement, $p = const./d_v$. Tracks detected in these three stations can be extrapolated backwards to $z = 0$[3] to also measure the transverse position of the interaction vertex.

[3]The coordinate system used in ZEUS has the z axis pointing in the proton beam direction, hereafter referred to as "forward", the x axis pointing horizontally toward the centre of HERA and the y axis pointing upwards. The polar angle θ is defined with respect to the z direction.

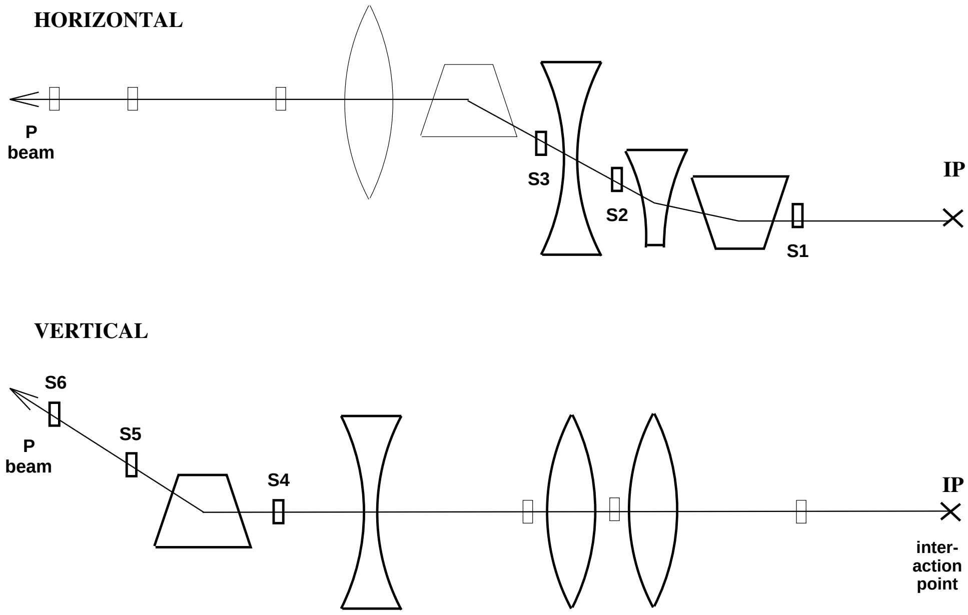

Fig. 8: Simplified LPS beam optics, where the beam elements have been grouped together to show the main optical function.

However, a method was developed for the case when only two stations are hit as a key to build up a viable acceptance; in this case, the interaction vertex position is used as a third point to measure the trajectory.

In a given projection, e.g. horizontal, the beam optics is described by a linear beam transport equation which relates the position h_k and the angle $h'_k = dh/dl$ of the track at each station to the position x_v and angle $x'_v = dx/dl$ of the track at the interaction vertex. Here l represents the coordinate along the nominal beam trajectory, while the positions and angles h and h' are relative to the nominal beam position and direction at that value of l (the nominal beam crosses the interaction vertex $z = 0$ at $x = y = 0$). One has:

$$\left[\begin{array}{c} h_k \\ h'_k \end{array}\right]_{z=z_k} = \left[\begin{array}{cc} T^k_{11}(x_L) & T^k_{12}(x_L) \\ T^k_{21}(x_L) & T^k_{22}(x_L) \end{array}\right] \left[\begin{array}{c} x_v \\ x'_v \end{array}\right]_{z=0} + \left[\begin{array}{c} B^k_1(x_L) \\ B^k_2(x_L) \end{array}\right] \quad (1)$$

An independent equation of the same form can be written for the vertical direction v. The transport matrix elements T^k are known functions of x_L which describe the effects of the beam quadrupoles and drift lengths. The vector elements B^k, also functions of x_L, describe the deflection induced by the beam dipoles and by the quadrupoles in which the beam is off axis; since the beam is taken as reference, they vanish as $x_L \to 1$.

Equation 1 and the corresponding one for the vertical direction can be written for a pair of stations (a,b); upon eliminating the unknowns x'_v and y'_v, one finds

$$\begin{array}{rclcl} h_b & = & m^{ab}_h(x_L)h_a & + & c^{ab}_h(x_L, x_v) \\ v_b & = & m^{ab}_v(x_L)v_a & + & c^{ab}_v(x_L, y_v) \end{array} \quad (2)$$

where m^{ab} and c^{ab} are known functions of the matrix elements T^k and B^k. Equations 2 are independent, apart from the common dependence on x_L. If drawn in the coordinates (h_a,h_b) and (v_a,v_b), they represent a set of lines with slope and intercept being a function of x_L. An example is shown in figure 9. For any pair of hits in stations a and b, two independent estimates of x_L can be obtained by determining on which of these lines the coordinates sit. Once x_L is determined, the equations 1 can be inverted to solve for x'_v and y'_v to give the transverse momentum.

Note that, as shown in figure 9, there are regions where lines of different x_L cross. The corresponding x_L ambiguity is resolved by comparing the x_L solutions found in this projection with those found in the

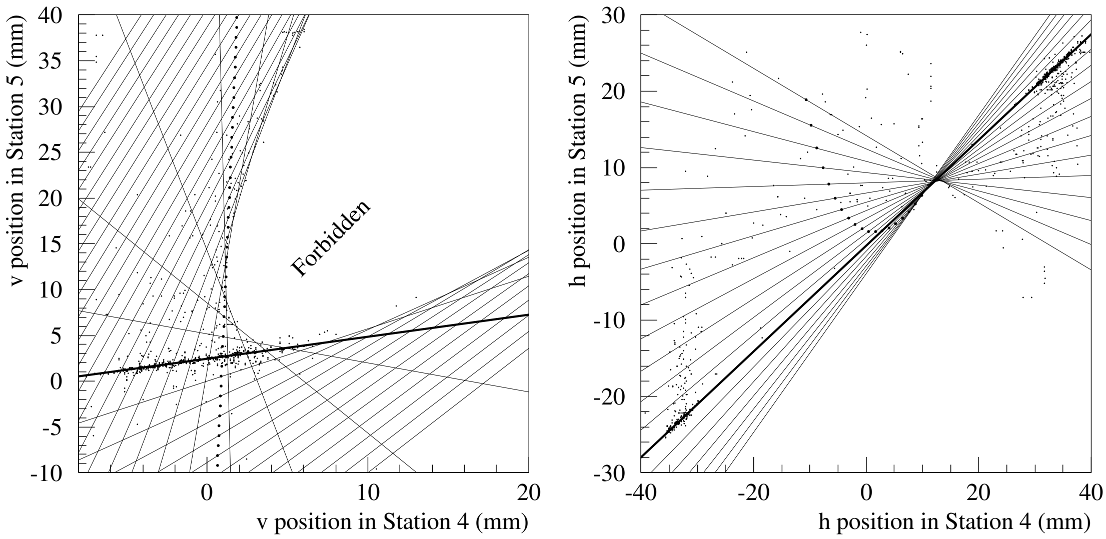

Fig. 9: Horizontal h and vertical v correlation between track positions in the two stations S4 and S5. Lines are for the correlations between the h and v coordinates measured in the two stations for tracks originating from the nominal interaction point. Each line corresponds to a fixed value of x_L, at intervals of fixed $1/x_L$, from 0.5 to 2. The thicker line is for $x_L = 1$ and the lines rotate clockwise as x_L decreases. The small dots are events and the large dots are the points on the fixed x_L lines where the transverse momentum p_x or p_y is zero. Diffractive physics shows up as the large fraction of events clustered around the $x_L = 1$ line.

other projection. Also, note that there are regions with no lines. Any pair of hits that reside in these forbidden regions cannot be caused by any track originating from the interaction point.

5.2 Track Reconstruction

To reconstruct tracks in the LPS, a pattern recognition is performed which is followed by a track fit [12, 13].

The task of the pattern recognition is to identify tracks in stages, starting with individual hits and gradually building to full tracks. Along the way, unlikely combinations of hits are eliminated. As several tracks can produce hits simultaneously in the detector, each track hitting up to 54 planes, this stage has to be carefully executed to avoid large combinatorial background or loss of track informations.
First, track segments are found independently in each detector assembly of six planes. Clusters of adjacent strips in each plane are matched between planes with the same strip orientation and combined with clusters (or matched clusters) belonging to the two other projections. In order to reduce the number of candidates, track segments that traverse the overlap region between the upper and lower halves of the stations are retained as a single candidate. All hits belonging to each candidate (up to twelve for tracks crossing the two halves, up to six otherwise) are used in a fit to find the transverse coordinates of the track at the z corresponding to the center of the station. Only the 10 best quality coordinates in each station are retained.

The next task is to combine from different stations pair of coordinates that belong to the same track. At initialization, the program calculates the transport matrices of equation 1 for each station at fixed values of x_L and stores the corresponding values in a lookup table. When comparing the h or v positions of two coordinates, the program builds the lines of equation 2 at intervals of x_L using the values stored in the lookup tables. The positions of the coordinates are then checked to see if they sit between two adjacent lines; if so, the distances to the two lines are used in a linear interpolation to determine the value of x_L. This process is illustrated in figure 10. In the regions of overlap (figure 10a) there may be more than one solution for x_L; only the value which is the closest to the solution found in the other

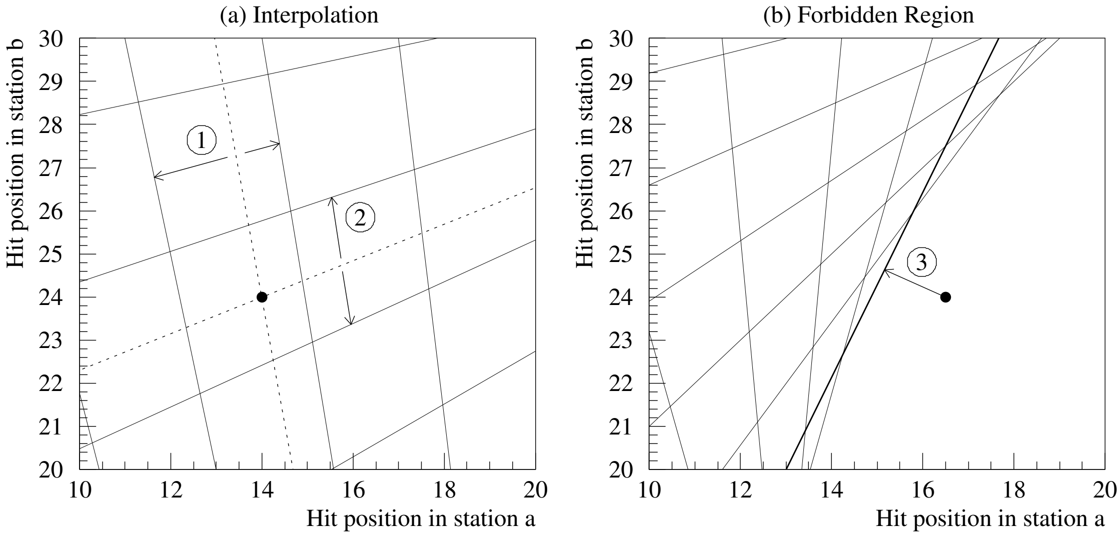

Fig. 10: Illustrating the two-station method of momentum reconstruction. The LPS reconstruction program generates a grid of lines of constant x_L from the lookup table. Most tracks (see large dot in **(a)**) produce hits that fall between these lines. In this case, x_L solutions are obtained by interpolating between adjacent neighboring lines as shown by ① and ②. For hits that fall in the forbidden region, the nearest line (dark line) is chosen as x_L solution ③.

projection is retained. The situation illustrated in figure 10b may instead occur if, for example, multiple scattering throws a track into the forbidden region; the x_L value of the closest line is chosen along with an appropriate error. Finally, the solutions found in the h and v projections are compared to make sure they are consistent within errors. If they are, the coordinate pair is saved as a two-station track candidate. As a final step of the pattern recognition, three-station track candidates are built by merging those two-station candidates which share the same hit in the station in common and whose x_L value is compatible within errors. Two-station and three-station candidates are then passed to a conventional track-fitting stage.

The track χ^2 is defined as

$$\chi^2 = \left[\sum_i \frac{[s_i - S_i(x_v, y_v, x'_v, y'_v, x_L)]^2}{\sigma_i^2} \right] + \frac{(x_v - x_0)^2}{\sigma_x^2} + \frac{(y_v - y_0)^2}{\sigma_y^2}, \tag{3}$$

where the sum runs over all clusters in all planes assigned to a track. Here s_i is the cluster position, σ_i the uncertainty associated to it (which includes the effects of multiple scattering and the contribution of the cluster width; typical values range from 50 to 100 μm), (x_0, y_0) are the nominal interaction vertex coordinates and σ_x and σ_y the nominal widths of the vertex distribution. S_i, a function of the five track parameters $(x_v, y_v, x'_v, y'_v, x_L)$, is the predicted cluster position calculated from equation 1 and the corresponding one for the vertical direction. The last two terms in equation 3 constrain the track to the interaction vertex. This expression, for simplicity, assumes that the cluster errors are uncorrelated, which is not true because of the contribution of the multiple scattering. The effect of this approximation is expected to be small.

This χ^2 is minimised with respect to the five track parameters, and the best track parameters, together with the error matrix, are determined. In addition to the χ^2 value, other quantities are assigned to each track candidate which allow to reject unphysical tracks. In particular, the miss probability $P_m = \prod(1 - \varepsilon_i)$, where the product extends over the planes missing a hit and where ε_i is the plane efficiency, is unlikely to be small for true tracks. Also, a detailed simulation of the shape of the beam elements allows to propagate the track through the beampipe and calculate the distance of closest approach to it; this quantity is required to be positive for all candidates.

5.3 Alignment and Calibration

The alignment is one of the most important and difficult problems. The parameters which affect the reconstruction are the magnetic fields of 23 beam elements (known with good accuracy), the positions of the quadrupole axes (known with less accuracy by the HERA survey), the positions of the LPS detectors and the position and tilt of the proton beam at the interaction vertex (all to be determined). In addition, the positions of the beam apertures are crucial in determining the acceptance of the detector. Furthermore, the spectrometer has some instabilities which are not under user control; these include vertex position and beam tilt in the interaction vertex, slow movements of the tunnel structure or even mechanical miscalibrations of the stations themselves. Fortunately, diffractive events provide a bright calibration line at $x_L = 1$. As an example, in elastic ρ^0 photoproduction $x_L \simeq 1 - (M_\rho^2 + |t|)/W^2$ where M_ρ is the ρ^0 meson mass and W is the photon-proton centre-of-mass energy; in these the value of x_L at HERA differs from unity on average by 10^{-4}.

The detailed description of the alignment procedure can be found in ref. [13, 14]; here we will briefly focus on the main issues.

The relative position of stations S4, S5 and S6 can be determined with a precision of few μm by using a sample of diffractive events (e.g. elastic ρ^0's) because the h and v projection of the $x_L = 1$ tracks are straight lines in the bending field between S4 and S5. Once these three stations are aligned relative to each other, the momentum of any three-station track can be determined by measuring the track deflection as discussed in section 5.1. A global fitting procedure was set in which the position of the three stations, considered as a rigid body was adjusted so that all three-station tracks of all momenta were seen to originate from a common minimized vertex volume. Care is taken in this stage to reject beam halo tracks which do not originate from the interaction vertex. Typical accuracy of this method is better than 20 μm. Adjustments to the position and the strengh of a quadrupole were also determined with this fit.

The next step is to determine where the beam lies in this reference frame as a key to measure the transverse momentum of the tracks relative to it. The procedure which follows was repeated for each fill of the machine. First, three-station tracks are fitted using equation 3 without constraining to the vertex and the average vertex position is determined. Then, the beam tilt at the interaction vertex is determined to within a few MeV by using diffractively photoproduced ρ^0 mesons ($\gamma p \to \rho^0 p$) and by requiring that the transverse momentum of the ρ^0, as measured in the central tracking chamber of ZEUS, is opposite to the transverse momentum of the scattered proton measured in the spectrometer.

Finally, the position of the limiting beam apertures is cross-checked with a precision of 0.2 mm by propagating a large sample of well reconstructed tracks at the location of the main obstructions.

Some distributions of reconstructed events are presented in the next section.

6 Some results

6.1 Resolution

Figure 11(left) shows the extrapolation accuracy with which the track positions at stations S5 and S6 of three-station tracks are used to predict the position at station S4 and the result is compared with the observed position at S4. After having carefully aligned the three stations, the horizontal projection is centered around zero while the vertical projection has a tail from events with $x_L < 1$. The single station resolution is a factor 1.7 narrower than the distribution which is shown. This indicates an effective average position resolution of about 35 μm under data taking conditions, consistent with the combined effect of detector resolution and stability of the mechanics as discussed in section 3.3.

Figure 11(right) shows the accuracy with which three-station tracks can be extrapolated back to the interaction vertex. Here diffractive events are fit without the vertex constraint (i.e. without the last two terms of equation 3) and the transverse vertex position resulting from the fit is plotted after subtracting the mean vertex position for that fill of the machine. The standard deviations of the distributions are 630 μm horizontally and 100 μm vertically, only about a factor 2 larger than the physical spot size of

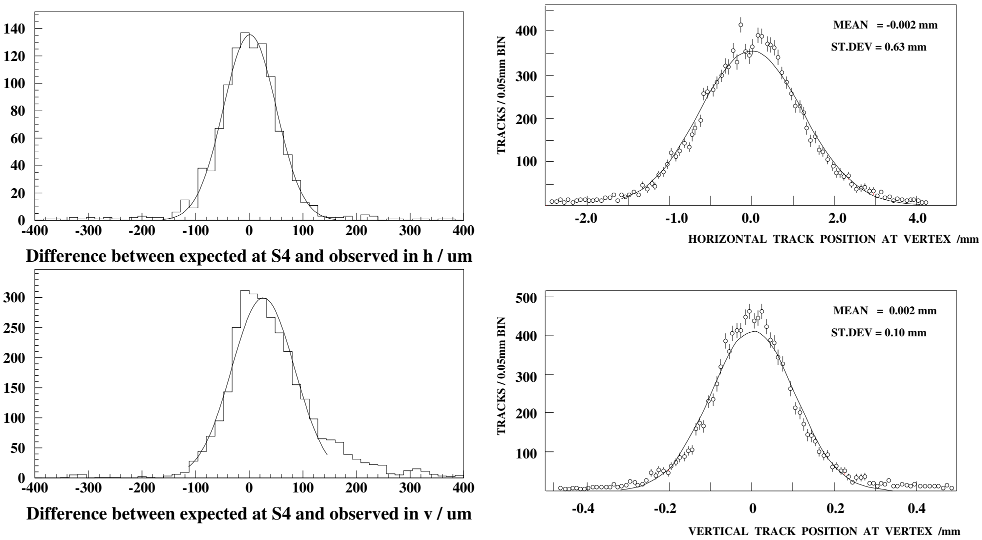

Fig. 11: Left: difference between the horizontal (above) or vertical (below) coordinate position in station S4 and that expected from the extrapolation from S5 and S6 in three-station tracks. Right: horizontal (above) and vertical (below) vertex distribution reconstructed with three-station tracks in the LPS. The lines show the result of a Gaussian fit to the distributions.

the interaction vertex and consistent with a design vertex resolution of 350 μm horizontally and 80 μm vertically.

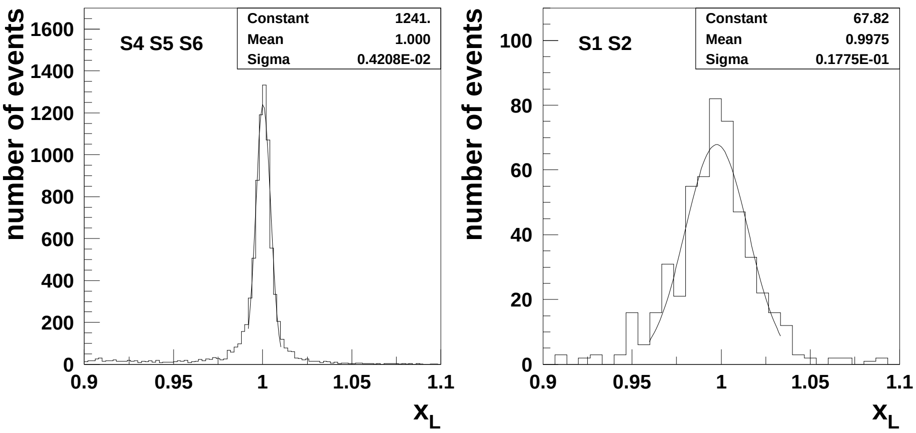

Fig. 12: Reconstructed x_L=1 line spectrum for elastic ρ^0 photoproduction events ($\gamma p \to \rho^0 p$). Left and right figures correspond to protons detected in stations S4→S6 and in stations S1-S2 respectively.

The x_L distributions of protons in elastic ρ^0 photoproduction events are shown in figure 12. As discussed in section 5.3, the width of these distributions correspond to the average resolution at $x_L = 1$; about 0.4% for tracks reconstructed in stations S4→S6 and about 2% for tracks reconstructed in the first three stations. These results match the expectations from Montecarlo studies. At lower momentum, the resolution is expected to worsen on average, although resolutions as good as 0.16% can be still achieved in some corners of the phase space [12].

The intrinsic transverse momentum resolution at $x_L = 1$ is about 5 MeV. This value is less than the transverse momentum spread of the proton beam at the interaction vertex (with rms of about 40 MeV horizontally and 95 MeV vertically) due to the emittance of the beam. This effect can be seen in figure 13 where the widths of the two distributions are largely dominated by the effect of the beam emittance. This limits the effective p_T resolution relative to the incoming proton to about 100 MeV in each event.

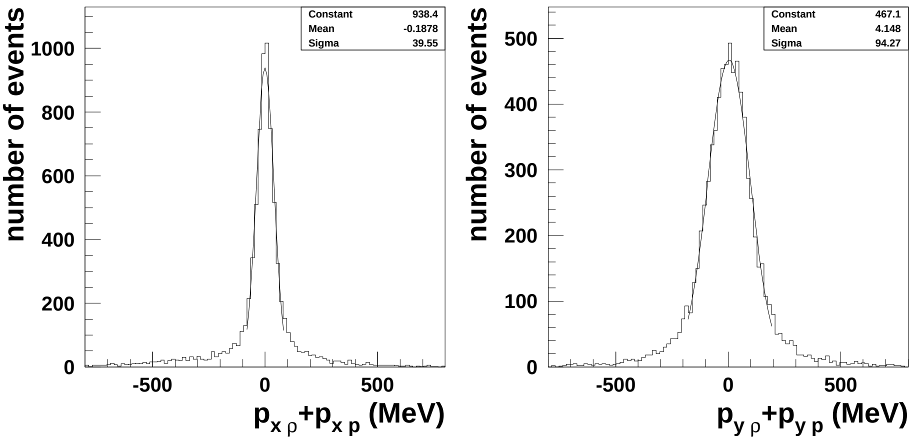

Fig. 13: Sum of horizontal and vertical components of the transverse momentum of the proton (measured with the LPS) and the ρ^0 meson (measured with the ZEUS tracking chambers) in $\gamma p \to \rho^0 p$ events. The lines show the result of a Gaussian fit to the distributions.

However, the beam emittance effect can be unfolded from cumulated distributions. An example will be discussed in section 6.3.

6.2 Correlation with the Central Detector

An effective way to demonstrate the role of the LPS is to show how it modifies our understanding of what is seen in the central detectors.

In figure 14, a scatter diagram of the pseudorapidity[4] η_{MAX} of the most forward energy deposit in the ZEUS calorimeter as a function of the fractional proton momentum x_L is shown for a sample of DIS events. The main group of diffractive events (regions A and B in the figure) is characterized by $x_L \simeq 1$ and a gap in rapidity in the central detector ($\eta_{\mathrm{MAX}} < 2$), and correspond to photon diffractive dissociation into a heavy mass state M_X. Following upwards at $x_L = 1$, the band curves in C toward lower x_L. This is because the higher η_{MAX} are associated with more massive diffractive states and therefore, being $M_X \propto \sqrt{1 - x_L - x_{bj}}$, the proton momentum is lower. These events are mostly diffractive but with hadrons in the proton hemisphere. Further over in the region D, η_{MAX} saturates because the forward beam-pipe hole prevents the true η_{MAX} measurement. This region correspond to non diffractive DIS with a leading proton emerging from the interaction. In the region E, the low η_{MAX} signals that the event is diffractive but $x_L < 1$ indicates that the proton lost a lot of energy. This is characteristic of proton diffractive excitation or dissociation into a low mass state.

The region F is anomalous and is attributed to a random coincidence of a genuine non-diffractive DIS event ($\eta_{\mathrm{MAX}} > 4$) and a beam halo proton ($x_L = 1$) or a soft pile-up event. These events can be identified by applying energy-momentum conservation, i.e. by requiring that the total measured $E{+}p_Z = (E + p_Z)_{\mathrm{Cal}} + 2x_L E_p$ is not larger than twice the proton beam energy E_p, where $(E + p_Z)_{\mathrm{Cal}}$ is the $E + p_Z$ measured in the ZEUS calorimeter. The $(E + p_Z)$ distributions of a sample of DIS events are shown in figure 15 (see figure caption for details). The probability of a random overlay of a beam halo track within the LPS acceptance was measured to be 0.25% in 1994 [14] and has increased starting in 1996 with the increase of the beam halo background produced by the HERA-B experiment. The residual halo background in diffractive analyses after the $(E + p_Z)$ cut is generally at the level of 5% and need to be subtracted statistically.

[4] The pseudorapidity η is defined as $-\ln(\tan\theta/2)$, where the polar angle θ is measured with respect to the proton beam direction.

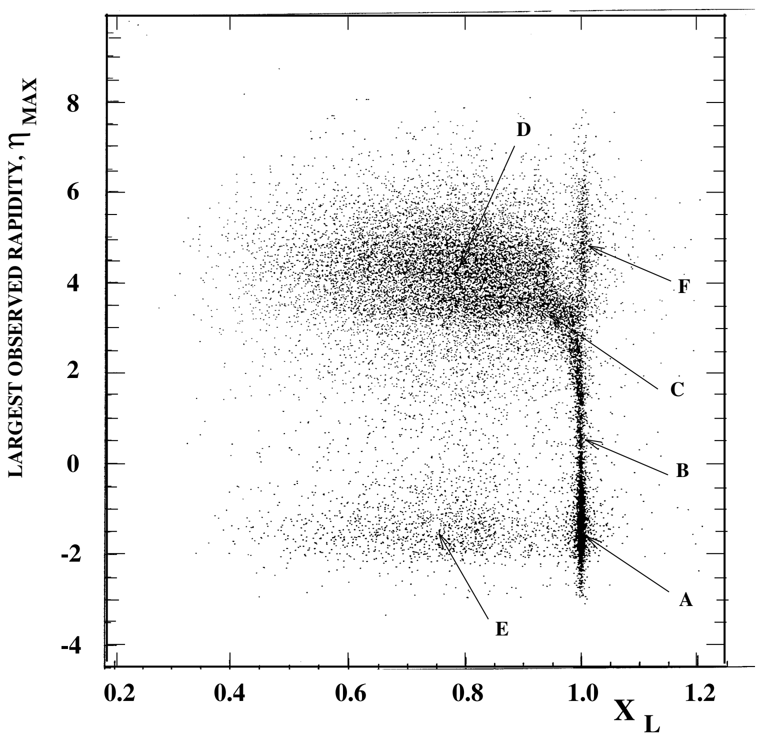

Fig. 14: Scatter diagram of $\eta_{\rm MAX}$ as a function of x_L for protons produced in DIS events. The different regions pointed by the arrows are explained in the text.

6.3 Diffractive Analyses using the LPS

Although limited by the small acceptance, the LPS is a valuable detector for diffractive analyses.

Figure 16 shows the x_L spectrum of DIS events. The well isolated x_L=1 peak allows the most clean and natural selection, independent from the hadronic final state, for various diffractive interactions. Compared to selection methods based on the features of the hadronic final state in the central detector, tagging the scattered proton eliminates the background of events with diffractive dissociation of the proton and allows to extend considerably the diffractive mass range up to masses of 50 GeV with little background contamination from non-diffractive processes.

The measurement of the proton in the LPS also provides the unique possibility of measuring the square of the four-momentum transfer at the proton vertex t in inclusive processes through the formula:

$$t = (p - p')^2 \approx -\frac{p_T^2}{x_L}[1 + (m_p^2/p_T^2)(x_L - 1)^2]$$

where p_T is the proton transverse momentum and m_p is the proton mass (in diffractive analyses, where $x_L \simeq 1$, t=$-p_T^2/x_L$ is normally a good approximation). The t acceptance in diffractive analyses can be determined directly from figure 7 and lies approximately in the range $0.07 \lesssim t \lesssim 0.45$ GeV^2. Important measurements like the diffractive structure function $F_2^{D(4)}$ and the slope b of the exponential fall-off of the t distribution were made possible through the use of the LPS [15, 16].
The t resolution at x_L=1 is approximately $\sigma(|t|) = 140\text{MeV}\sqrt{|t|}$ (t in GeV^2) and is mainly affected by the angular beam spread due to the beam emittance discussed in section 6.1. However, the effect of the beam emittance can be unfolded from the observed p_T^2 distribution with various techniques. Alternatively, the slope b can be determined by fitting the p_T^2 distribution with the convolution of an exponentially falling distribution with slope b and a two-dimensional Gaussian distribution representing the

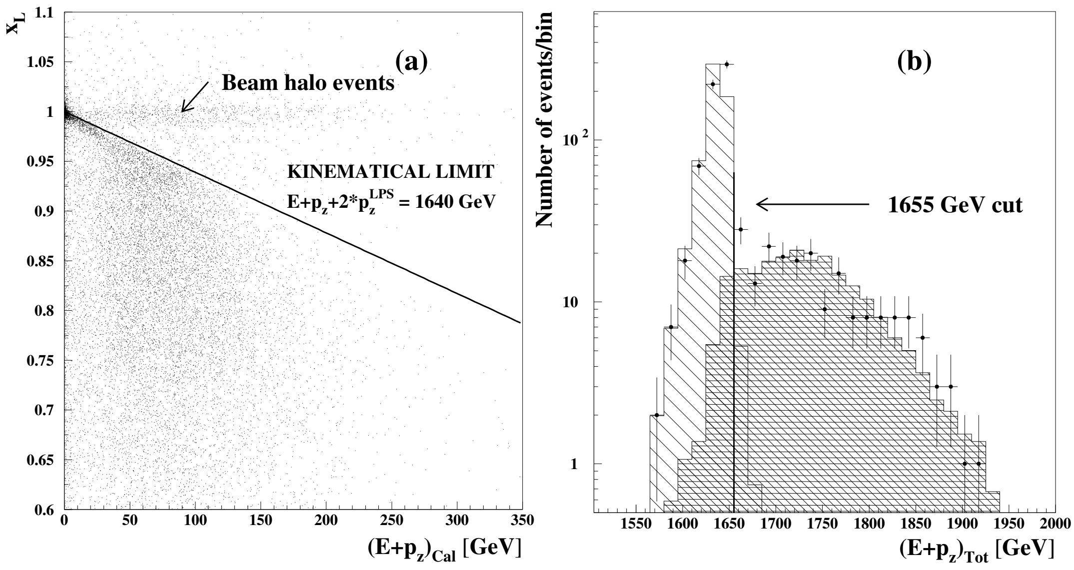

Fig. 15: (a) Scatter plot of x_L versus the $(E+p_Z)_{\mathrm{Cal}}$ measured in the ZEUS calorimeter; the region below the solid line indicates the allowed kinematic region. (b) Total $(E+p_Z)$ distribution for a sample of DIS data; the two shaded histograms represent the diffractive signal from Montecarlo simulation and the distribution of random overlays of a DIS event and a beam halo proton. In both figures, the events were collected with a proton beam energy E_p=820 GeV. The cut on $(E+p_Z)$ is set at 1655 GeV in figure (b) to account for the LPS resolution.

beam transverse momentum distribution, with standard deviations σ_{p_x} and σ_{p_y}; one finds

$$\frac{d\sigma}{p_T^2} \propto \pi \exp\left\{b[1-(\sigma_{p_x}^2+\sigma_{p_y}^2)b]p_T^2\right\} \cdot I_0\left[(\sigma_{p_y}^2-\sigma_{p_x}^2)b^2p_T^2\right]$$

where $I_0(z)$ is the modified Bessel function of order 0 [12].

The use of the LPS also provides an indirect way to measure the diffractive mass M_X in DIS by the missing mass method:

$$M_X^2 = (1-x_L)(W^2+Q^2-m_p^2) - Q^2 + t$$

where W is the photon-proton center-of-mass energy and Q^2 is the photon virtuality. The M_X resolution obtained with this method is comparable with that obtained directly from the hadronic final state for $M_X > 10$ GeV, but worsens rapidly as the mass decreases. However, unlike the direct measurement, no correction factor is needed to compensate the effect of energy loss in the dead material of the central detector [15].

Finally, the measurement of the final state proton with the LPS allows to determine the azimuthal angle Φ between the electron and the proton scattering planes in the $\gamma^* p$ frame [16]. In some models, the distribution of this azimuthal angle is expected to bear important informations about the nature of the diffractive interaction.

7 Conclusions

The Leading Proton Spectrometer was the first Roman pot system installed at HERA. It was integrated in the ZEUS experiment and was operated continuously from 1994 to year 2000, before the upgrade of the HERA straight section took place. It featured six detector stations which made use of position-sensitive microstrip detectors to measure protons scattered into the HERA beampipe; during data taking, the detectors were positioned as close as few millimeters from the circulating proton beam. In total,

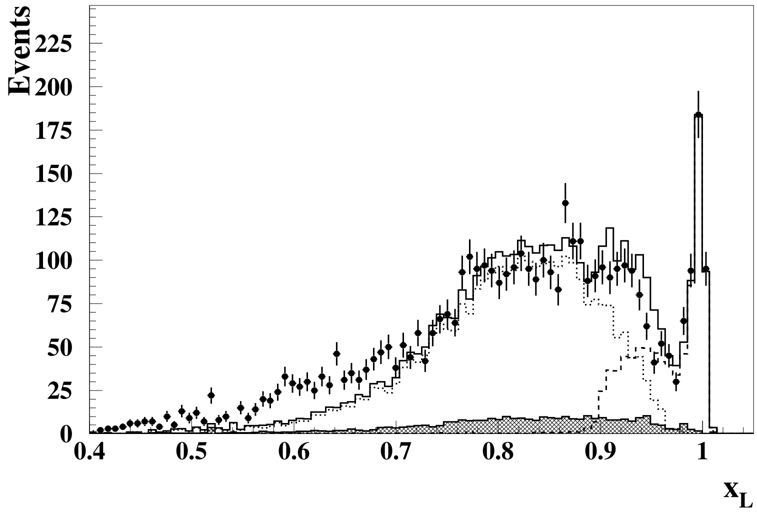

Fig. 16: The observed x_L spectrum of DIS events (dots). Overlaid is the result of fitting the distribution with a sum (full line) of the contribution due to proton dissociation (shaded area), of pion exchange (dotted line) and of the single photon diffractive dissociation (dashed line).

the system featured about 54000 readout channels which were all read out synchronously with the 10 MHz frequency of the HERA bunch crossing. Among the other features of this detector are a mechanical system which allows both an automated controlled insertion of the detectors into the beam pipe and a fast safety extraction, and a trigger system for diffractively scattered protons. The high data taking efficiency allowed to collect over 70 nb^{-1} of integrated luminosity in six years of operations.
A well designed reconstruction method and a precise alignment of the detector allowed to reach the design momentum resolution of 0.4% for full momentum tracks with a reconstruction efficiency well above 90%.
Although limited by the low acceptance, the data collected allow for a wide range of applications. In particular for diffraction, they allow a clean and natural selection of diffractive events and offer the unique possibility to measure the squared four-momentum t exchanged at the proton vertex.

The success of the LPS was a result of a team effort of several institutes leaded by Tom Massam (INFN Bologna): University departments and INFN sections of Bologna, Cosenza and Torino, LAA, Wordlab and University of Santa Cruz. The collaboration with the LPS group of several ZEUS members and HERA engineers has also been crucial for the construction and the operations of the detector.

References

[1] M. Basile et al., Lettere al Nuovo Cimento **41**, 298 (1984).

[2] U. Amaldi et al., Phys. Lett. **B 43**, 231 (1973).

[3] ZEUS Coll., U. Holm (ed.), *The ZEUS Detector*. Status Report (unpublished), DESY, 1993, available on `http://www-zeus.desy.de/bluebook/bluebook.html`.

[4] E. Barberis et al., Nucl. Instr. and Meth. **A 364**, 507 (1995).

[5] D.E. Dorfan, Nucl. Instr. and Meth. **A 342**, 143 (1994).

[6] E. Barberis et al., Nucl. Phys. **B 32**, 513 (1993).

[7] J. DeWitt, Nucl. Instr. and Meth. **A 288**, 209 (1990).

[8] J. DeWitt, *The Time Slice Chip*. Senior Thesis, UC Santa Cruz, 1989.

[9] A. Staiano, Nucl. Phys. **B 54**, 125 (1997).

[10] R. Battiston et al., Nucl. Instr. and Meth. **A 238**, 35 (1985).

[11] S. Bhadra et al., Nucl. Instr. and Meth. **A 394**, 121 (1997).

[12] R. Sacchi, *Studio di eventi diffrattivi con uno spettrometro per protoni a ZEUS*. Tesi di Dottorato, University of Torino, 1996.

[13] J. Rahn, *Studying Characteristics of Diffractive Deep Inelastic Scattering with the ZEUS Leading Proton Spectrometer*. PhD Thesis, UC Santa Cruz, 1997.

[14] ZEUS Collaboration, M. Derrick et al., Z. Phys. **C 73**, 253 (1997).

[15] ZEUS Collaboration, M. Derrick et al., Eur. Phys. J. **C 1**, 81 (1998).

[16] ZEUS Collaboration, S. Chekanov et al., Eur. Phys. J. **C 38**, 43 (2004).